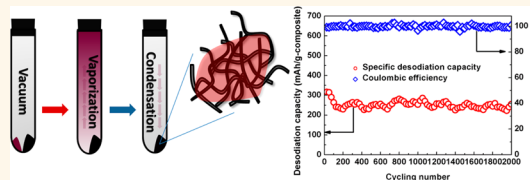


Red Phosphorus—Single-Walled Carbon Nanotube Composite as a Superior Anode for Sodium Ion Batteries

Yujie Zhu,[†] Yang Wen,[†] Xiulin Fan,[†] Tao Gao,[†] Fudong Han,[†] Chao Luo,[†] Sz-Chian Liou,[‡] and Chunsheng Wang^{*,†}

[†]Department of Chemical and Biomolecular Engineering, University of Maryland, College Park, Maryland 20742, United States and [‡]Maryland Nanocenter, University of Maryland, College Park, Maryland 20742, United States

ABSTRACT Sodium ion batteries (SIBs) have been considered as a top alternative to lithium ion batteries due to the earth abundance and low cost of sodium compared with lithium. Among all proposed anode materials for SIBs, red phosphorus (P) is a very promising candidate because it has the highest theoretical capacity (~ 2600 mAh/g). In this study, a red P—single-walled carbon nanotube (denoted as red P—SWCNT) composite, in which red P is uniformly distributed between tangled SWCNTs bundles, is fabricated by a modified vaporization-condensation method. Benefiting from the nondestructive preparation process, the highly conductive and mechanically strong SWCNT network is preserved, which enhances the conductivity of the composite and stabilizes the solid electrolyte interphase. As a result, the red P—SWCNT composite presents a high overall sodium storage capacity (~ 700 mAh/g_{composite} at 50 mA/g_{composite}), fast rate capability (~ 300 mAh/g_{composite} at 2000 mA/g_{composite}), and stable long-term cycling performance with 80% capacity retention after 2000 sodiation—desodiation cycles. The red P—SWCNT composite fabricated by the vaporization—condensation method significantly extends the cycling stability of P/carbon composite from current ~ 100 cycles to ~ 2000 cycles.



KEYWORDS: sodium ion batteries · anode · phosphorus · carbon nanotubes

Lithium ion batteries (LIBs) currently dominate the power supply for portable electronic devices and have been integrated into (plug-in hybrid) electric vehicles to reduce the energy dependence on fossil fuels.¹ Considering the massive consumption of LIBs in the future, cost will become one of the major issues for LIBs due to the very limited and unevenly distributed lithium resources.² Thus, alternative energy storage systems with low cost will be urgently needed for future applications. Recently, room temperature sodium ion batteries (SIBs) have attracted an intensive attention and been considered as a potential alternative to LIBs because of the earth abundance and low cost of sodium compared with lithium.^{3–5} It is reported that the relative earth abundance of sodium in crust is more than 1000 times higher than that of lithium (23600 ppm for sodium vs 20 ppm for lithium).⁶ Given the similarity between lithium and sodium chemistry, an intuitive idea is to directly transfer well-developed electrode materials in LIBs to SIBs with the

replacement of lithium by sodium. Unfortunately, the most common and commercially successful graphite anode for LIBs was proven to only store a very little amount of sodium due to the insufficient interlayer distance and stretched C—C bond induced by sodiation,^{7–10} which makes the Na-graphite intercalation compound thermodynamically unstable. Therefore, a diversity of alternative materials,¹¹ including nongraphitized carbon,^{12–15} metal oxides,^{16–18} and alloy-based materials,^{19–24} have been explored as potential anodes for SIBs. Among all proposed anode materials, red phosphorus (P) is a very promising candidate because it has the highest theoretical sodium storage capacity (~ 2600 mAh/g, based on the assumption that P is transformed to Na_3P) and a relatively safer operating potential (~ 0.45 V vs Na/Na^+) than other materials (for example, hard carbon which has a sodiation potential close to 0 V vs Na/Na^+).²⁵ However, the application of red P in SIBs is handicapped by two factors. First, pristine amorphous red P has

* Address correspondence to cswang@umd.edu.

Received for review January 17, 2015 and accepted March 4, 2015.

Published online March 04, 2015
10.1021/acsnano.5b00376

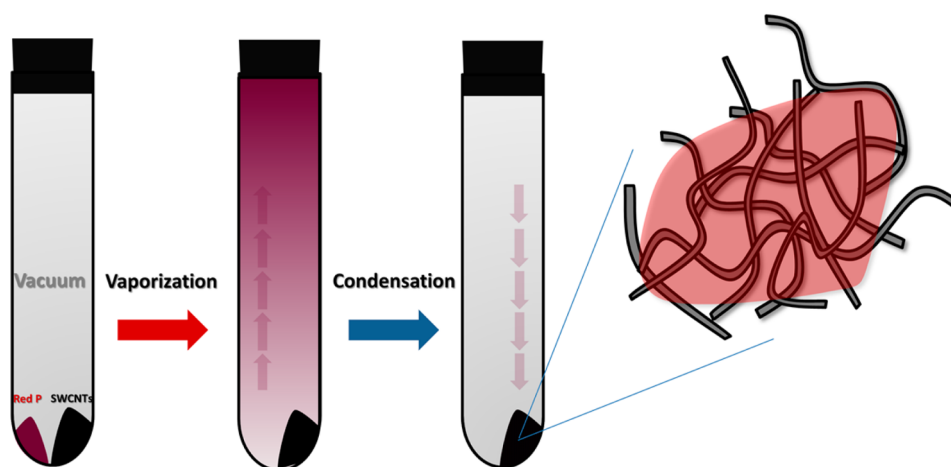
© 2015 American Chemical Society

a very low electrical conductivity ($\sim 10^{-14}$ S/cm),²⁶ resulting in large polarizations and a low utilization of active material. Second, the large volume change ($\sim 300\%$) of red P during sodiation/desodiation will cause severe pulverization of active material and loss of electrical contact between active material and current collector/conductive additive, leading to capacity decay.^{27–29} Similar to the well-known silicon anode in LIBs,^{30,31} the repeated volume changes will also generate unstable, thick, and electronically insulating solid electrolyte interphase (SEI) film between active material and electrolyte, hindering the reaction kinetics and giving rise to capacity degradation and low Coulombic efficiency.²⁹ To circumvent these two limitations, red P was often mixed with carbon to form amorphous P–carbon composites.^{27,28,32} The amorphous P–carbon composites were usually prepared by high-energy mechanical ball milling of carbon sources (e.g., carbon black, graphene) and red P, during which red P was transformed into well-dispersed amorphous P clusters embedded in the carbon matrix. In this way, carbon matrix was able to enhance the electrical conductivity of the composites and the amorphous structure of P could accommodate the volume changes during sodiation/desodiation.²⁷ Consequently, the electrochemical performance of P was greatly improved. As simultaneously and independently reported by Yang *et al.*²⁷ and Lee *et al.*,²⁸ the amorphous P–carbon composites have demonstrated a very high reversible sodium storage capacity (>1500 mAh/g_P) and much better reversibility compared with pristine red P. Yang *et al.*²⁷ have shown that the reversible sodium storage capacity of the amorphous P–carbon composite was around 1500 mAh/g_P and maintained stable during the initial 20 cycles in the electrolyte with fluoroethylene carbonate (FEC) additive. However, the capacity gradually decreased to 1000 mAh/g_P at the 80th cycle. A slightly higher reversible capacity of 1890 mAh/g_P was reported by Lee *et al.*²⁸ for their ball-milled amorphous P–carbon material. When using poly(acrylic acid) (PAA) as the binder, less than $\sim 7\%$ capacity decay was observed during the reported 30 cycles and good rate capability was achieved (~ 1540 mAh/g_P at a current density of 2.86 A/g_P). Very recently, Wang *et al.*³² developed a chemically bonded P/graphene hybrid, prepared through high energy ball milling of red P and graphene stacks, as a high performance anode for SIBs. Phosphorus was shown to chemically bond with the graphene, and the amorphous P/graphene hybrid presented much-improved electrochemical performance (~ 1700 mAh/g_P after 60 cycles) compared with the ball-milled P/carbon black material (~ 709 mAh/g_P after 60 cycles), suggesting that the choice of carbon played a critical role in stabilizing P anode.

Besides the amorphous P–carbon composites generated by high energy ball milling, Dou *et al.*³³ recently

reported that, by simply mixing commercial micro-sized red P with multi-walled carbon nanotubes (MWCNTs) through hand-grinding, crystalline red P could deliver a surprisingly high initial capacity of 1530 mAh/g_P. Although the reported red P–MWCNT composite showed a significantly higher reversible capacity and much more improved cyclability compared with pristine red P, the capacity of the composite dropped from 1530 to 750 mAh/g_P after only 20 cycles, limiting the practical application of the red P–MWCNTs composite.

Herein, inspired by the pioneering work of Dou *et al.*³³ which demonstrated that carbon nanotubes could be an excellent carbon source to stabilize P anode, we report a red P–single-walled carbon nanotube (SWCNT) (denoted as red P–SWCNT) composite, in which red P is uniformly distributed between tangled SWCNT bundles, as a very promising anode for SIBs. Here we choose SWCNTs over MWCNTs because SWCNTs possess a higher average Young's modulus (320–1470 GPa for SWCNT vs 270–950 GPa for MWCNT) and larger average tensile strength (3.6 GPa for SWCNT vs 1.72 GPa for MWCNT),^{34–37} which are expected to benefit the cycling stability during sodiation/desodiation. Different from previous P–carbon composites prepared by high energy ball/hand milling of red P and carbon sources, the red P–SWCNT composite is prepared by a vaporization–condensation method, which was previously introduced by Monconduit *et al.*³⁸ and He *et al.*³⁹ to prepare P/carbon composites for LIBs anode. Different from previous reports,^{38,39} a modified vaporization–condensation method, in which a higher temperature and vacuum condition are used, is applied in the current study. Thus, a large driving force will be created for P vapor to easily diffuse into the empty spaces between tangled SWCNTs bundles, ensuring the well dispersion of red P between SWCNTs bundles. Taking advantage of this mild and nondestructive preparation method, the highly conductive and mechanically strong SWCNT network is preserved for the red P–SWCNT composite. As a result, the red P–SWCNT composite presents excellent electrochemical performance toward sodium storage with a high overall reversible capacity, fast sodiation–desodiation capability, and great electrochemical performance under various current densities, *i.e.*, almost no capacity decay for cells cycled at 50 and 500 mA/g_{composite} during the reported cycles, and 80% capacity retention after 2000 sodiation–desodiation cycles at 2000 mA/g_{composite}. To the best of our knowledge, this is the best electrochemical performance reported so far for phosphorus anode in SIBs. Detailed studies reveal that the improved electrochemical performance of red P–SWCNT composite compared with the red P/SWCNT mixture prepared by hand-grinding is attributed to the uniform mixing and intimate contact



Scheme 1. Schematic illustration of the synthesis process for red P–SWCNT composite.

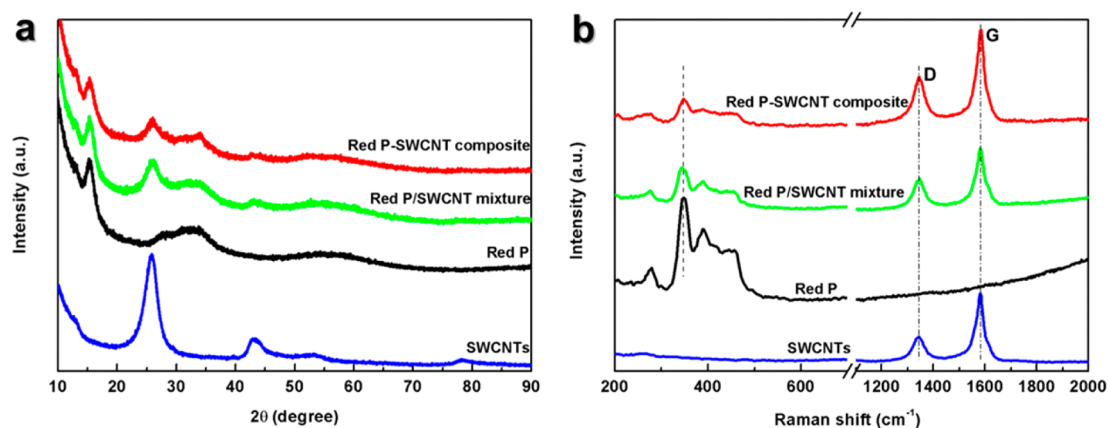


Figure 1. (a) XRD and (b) Raman spectra for different materials.

between red P and SWCNTs, which increase the electrical conductivity of the composite and decrease the charge transfer resistance. Moreover, electrochemical impedance spectroscopy study indicates that the SWCNTs enable a stable interface between electrolyte and composite, realizing stable long-term electrochemical cycling.

RESULTS AND DISCUSSION

Scheme 1 schematically illustrates the synthesis process of red P–SWCNT composite. The red P–SWCNT composite is prepared by a modified vaporization–condensation method. Red P and SWCNTs are first sealed in a glass tube under vacuum condition. Then, the glass tube is heated to 600 °C and held at this temperature. After the glass tube naturally cools down to room temperature during which P vapor condenses between the SWCNT bundles, the red P–SWCNT composite is obtained by washing and drying the collected powder (see Methods section for more details).

Figure 1a shows the XRD patterns for SWCNTs, commercial red P, red P/SWCNT mixture prepared by hand-grinding for 15 min, and red P–SWCNT composite. For the SWCNTs, two peaks centered at $2\theta \sim 26^\circ$

and $\sim 43^\circ$ correspond to the reflection of graphitic planes of SWCNTs.⁴⁰ The XRD pattern of commercial red P is similar to the one reported in the literature with the first sharp peak centered at $2\theta \sim 15^\circ$, indicating a medium-range ordered structure.^{41,42} The XRD pattern of red P/SWCNT mixture is simply the combination of XRD patterns of SWCNTs and commercial red P. The XRD pattern of the red P–SWCNT composite resembles that of the red P/SWCNT mixture without any detectable new peak, implying that no crystalline impurity is generated during the preparation process. Different from the XRD patterns of P–carbon composites prepared by high energy ball milling, in which the diffraction peaks corresponding to red P completely disappeared,^{27,32} the red P peak centered at $2\theta \sim 15^\circ$ can still be clearly observed in our red P–SWCNT composite, indicating the crystalline structure of red P is not completely destroyed during the preparation process. Figure 1b shows the Raman spectra for the samples. SWCNTs show a weak D band at 1345 cm^{-1} and a strong G band at 1582 cm^{-1} , indicating a highly graphitic structure. Pristine red P presents three major peaks between 300 and 500 cm^{-1} , consistent with the Raman spectrum reported in the literature.⁴³ For both

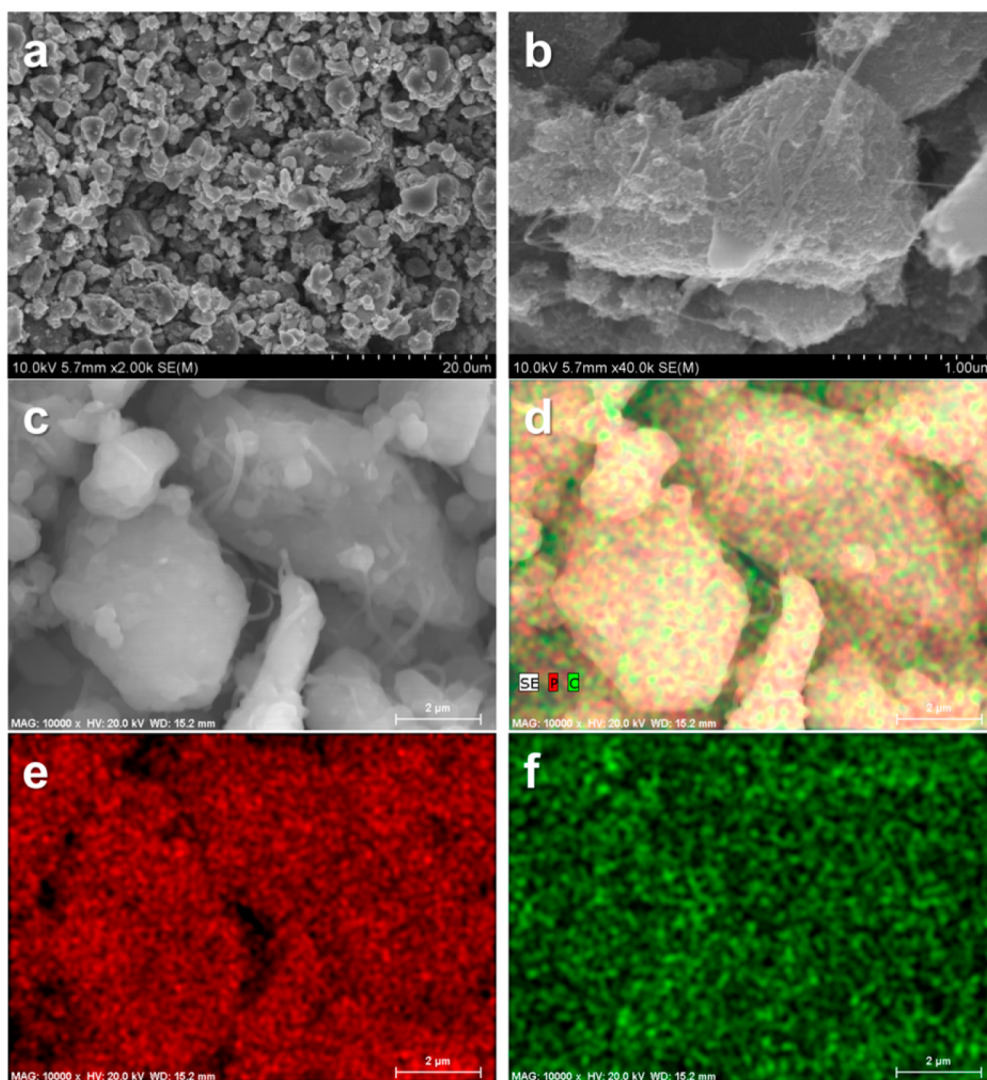


Figure 2. (a–c) SEM images of red P–SWCNT composite. (d–f) EDS elemental mapping of (d) phosphorus and carbon, (e) phosphorus, and (f) carbon for the red P–SWCNT composite particles shown in (c).

red P–SWCNT composite and red P/SWCNT mixture, signals corresponding to red P and SWCNTs are clearly detected. The intensity ratio of the D band to the G band is similar between red P–SWCNT composite and red P/SWCNT mixture, and no peak shift is observed for both SWCNTs and red P in the red P–SWCNT composite compared with red P, SWCNTs, and red P/SWCNT mixture, which might indicate that there is no surface interaction between red P and SWCNTs in the composite.^{32,33} The peak intensity of red P is decreased in the red P–SWCNT composite compared with that in the red P/SWCNT mixture, probably because red P is partially covered by SWCNTs as evidenced by scanning electron microscopy (SEM) images (Figure 2).

Supporting Information Figure S1 shows the SEM and transmission electron microscopy (TEM) images of pristine SWCNTs. At low magnification, pristine SWCNTs present an irregular shape with tens of micrometers (Supporting Information Figure S1a). Under

high magnification, individual SWCNT bundles can be observed and these bundles are loosely entangled with empty space between them (Supporting Information Figure S1b). As shown by the TEM images (Supporting Information Figure S1c,d), the pristine SWCNT bundles make contact with each other to form a network. Figure 2 shows the SEM images of the red P–SWCNT composite. After the vaporization–condensation process, the average particle size of red P–SWCNT composite is around $5.0\ \mu\text{m}$ (Figure 2a). In contrast to the loose structure of pristine SWCNTs, the red P–SWCNT composite appears much denser and several SWCNT bundles can be clearly observed on the surface of the composite (Figure 2b), implying that red P is filled into the empty space between SWCNT bundles and suggesting a high tap density. Elemental mapping by the SEM energy dispersive X-ray spectrometry (EDS) (Figure 2d–f) demonstrates that carbon and P are uniformly mixed with each other in the composite, ensuring a high electronic conductivity for the

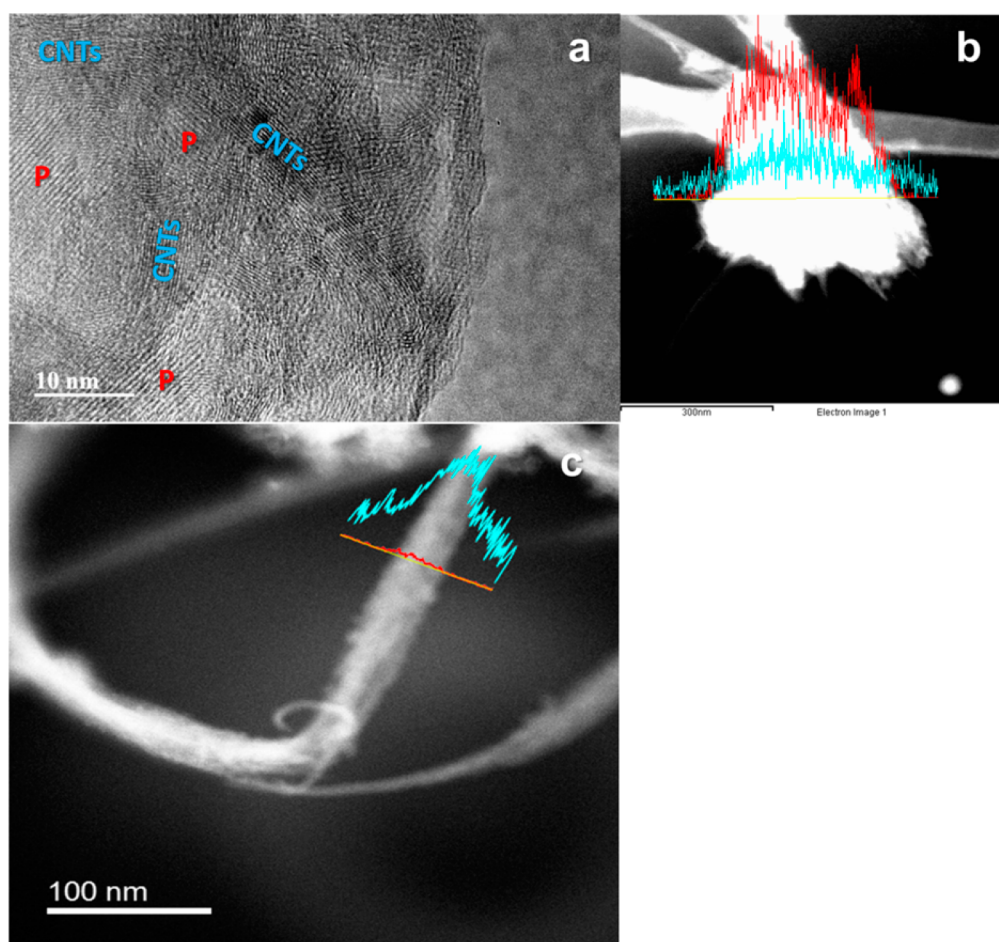


Figure 3. (a) High resolution TEM image of red P–SWCNT with P and carbon nanotubes (CNTs) marked according to their different crystalline lattices. EDS line scan of (b) one red P–SWCNT composite particle and (c) a bundle of SWCNTs in the composite (P signal is red and carbon signal is blue).

composite. For the red P/SWCNT mixture prepared by hand-grinding, EDS elemental mapping in Supporting Information Figure S2 shows that microsized P particle is isolated from SWCNTs. TEM is used to investigate the interior structure of red P–SWCNT composite. As shown by the high resolution TEM image in Figure 3a, the crystalline lattices of SWCNTs and red P can be observed, and SWCNTs are randomly distributed around red P domains to form a conductive network. The TEM EDS line scanning in Figure 3b demonstrates the existence and continuous distribution of SWCNTs across a composite particle. To investigate the distribution of P inside the SWCNT bundles, the TEM EDS line scanning across a bundle of SWCNTs is performed and the result (Figure 3c) shows very weak P signal, implying that very limited amount of P is stored inside the SWCNT bundles.

Figure 4 shows the electrochemical performance of different samples. Unless otherwise specified, both capacity and current density reported in this work are calculated on the basis of the overall weight of red P–SWCNT composite or red P/SWCNT mixture. Figure 4a shows the cyclic voltammetry (CV) result

of the initial five scans for red P–SWCNT composite at a scan rate of 0.05 mV/s between 0.001 and 2 V (vs Na/Na⁺). A broad peak around 1.0 V (vs Na/Na⁺) is observed during the first cathodic scan, which is attributed to the reduction of electrolyte to form the SEI layer. In the subsequent cathodic scans, instead of the peak around 1.0 V (vs Na/Na⁺), a weak peak around 0.92 V (vs Na/Na⁺), which overlapped with the SEI peak in the first cathodic scan, is observed and could be ascribed to the initial sodiation of red P. Starting from the third cathodic scan, a peak around 0.35 V (vs Na/Na⁺) is developed and the peak intensity gradually increases from the third scan to the fifth scan, indicating gradually enhanced sodiation kinetics. When the voltage is scanned close to 0.001 V (vs Na/Na⁺), the current increases sharply and an incomplete peak is developed around 0.001 V (vs Na/Na⁺), corresponding to further sodiation of red P. During all five anodic scans, a strong peak around 0.63 V (vs Na/Na⁺) with a shoulder around 0.71 V (vs Na/Na⁺) and a weak peak around 1.4 V (vs Na/Na⁺) are observed, which should be attributed to the desodiation of different Na_xP compounds. It is

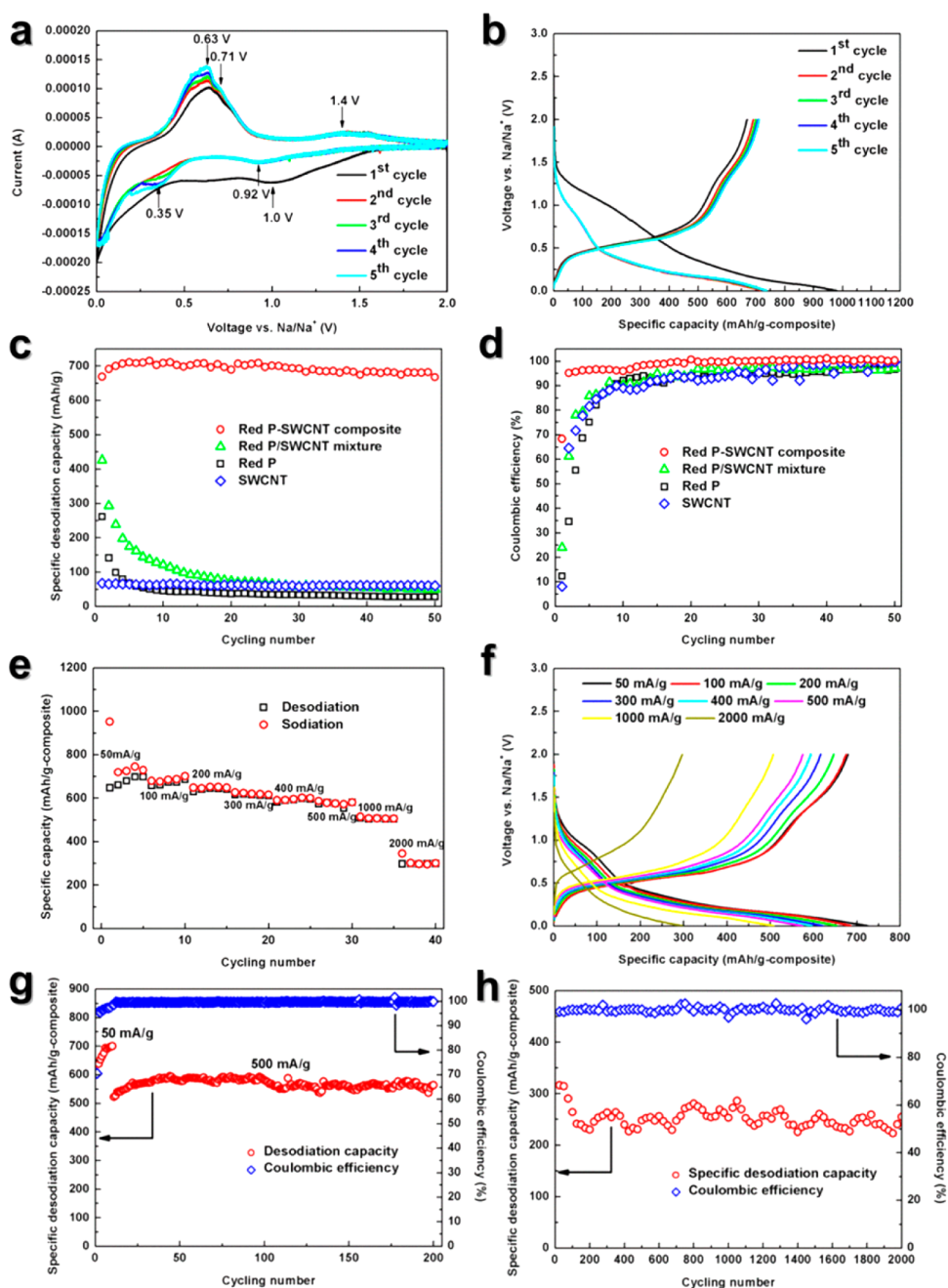


Figure 4. Electrochemical performance of red P–SWCNT composite. (a) Cyclic voltammetry of red P–SWCNT between 0.001 and 2 V (vs Na/Na^+) at a scanning rate of 0.05 mV s^{-1} . (b) Galvanostatic charge–discharge voltage profiles of red P–SWCNT composite during the first 5 cycles at a current density of $50 \text{ mA/g}_{\text{composite}}$. (c) Cycling performance and (d) Coulombic efficiency of red P–SWCNT composite, red P/SWCNT mixture hand-milled for 15 min, red P, and SWCNTs at a current density of 50 mA/g . (e) Sodiation/desodiation capacity and (f) voltage profiles of red P–SWCNT composite at different current densities. (g) Cycling performance of red P–SWCNT composite at $50 \text{ mA/g}_{\text{composite}}$ with initial 10 cycles performed at $50 \text{ mA/g}_{\text{composite}}$. (h) Cycling performance of red P–SWCNT composite at $2000 \text{ mA/g}_{\text{composite}}$ with desodiation capacities at the 25th, 50th, 75th, ..., 2000th cycle are plotted. Note: for red P–SWCNT composite and red P/SWCNT mixture, both current densities and specific capacities are calculated on the basis of the total weight of red P–SWCNT composite or red P/SWCNT mixture. For red P and SWCNTs, both current densities and specific capacities are calculated on the basis of the weight of red P or SWCNTs.

obvious that, for the peak located at 0.63 V (vs Na/Na^+), the peak current increases and the peak potential slowly shifts to lower voltages from the first scan to the fifth scan, implying that the desodiation kinetics are also gradually improved during cycling. Figure 4b presents the sodiation–desodiation curves of the

initial five cycles for red P–SWCNT composite under a constant current density of $50 \text{ mA/g}_{\text{composite}}$. Except for the first sodiation curve which is different from others due to the SEI formation, the general sodiation curves consist of a sloping region from 1.5 to 0.5 V (vs Na/Na^+) followed by an inclined plateau from

0.5 to 0.11 V (vs Na/Na⁺) and another sloping region from 0.11 to 0.001 V (vs Na/Na⁺). Correspondingly, the desodiation curves comprise a sloping region from 0.07 to 0.37 V (vs Na/Na⁺) and an inclined plateau from 0.37 to 0.8 V (vs Na/Na⁺) followed by a sloping region up to 2 V (vs Na/Na⁺).

Figure 4c shows the variation of desodiation capacity for red P–SWCNT composite at 50 mA/g_{composite} for 50 cycles. For comparison, the cycling performance of red P, SWCNTs and red P/SWCNT mixture under the same current density is also presented in Figure 4c with the sodiation–desodiation curves of those samples shown in Supporting Information Figure S3. Pristine red P has a sodiation capacity over 2000 mAh/g_P in the first cycle (Supporting Information Figure S3a). However, the first desodiation capacity is only 250 mAh/g_P and decreases to below 50 mAh/g_P after only 10 cycles (Figure 4c). Compared to pristine red P, the red P/SWCNT mixture prepared by hand-grinding shows an increased first cycle desodiation capacity of 430 mAh/g_{mixture} (Figure 4c and Supporting Information Figure S3b), which corresponds to 985 mAh/g_P given SWCNTs can provide a stable desodiation capacity of 60 mAh/g_{SWCNTs} (Figure 4c and Supporting Information Figure S3c) and the weight ratio between red P and SWCNTs is 4:6 in the mixture, but its cycling performance is still very poor with a drop in desodiation capacity to 100 mAh/g_{mixture} (~160 mAh/g_P) at the 20th cycle (Figure 4c). It should be mentioned that the electrochemical performance of the red P/SWCNT mixture in present study is poorer than that of reported red P–MWCNTs,³³ probably due to the shorter hand-grinding time used in the present work (15 min in Figure 4c vs 1 h in ref 33). As shown in Supporting Information Figure S3d, the electrochemical performance of red P/SWCNT mixture could be improved when the hand-grinding time was extended. For the red P–SWCNT composite with the same P content (~40 wt % as determined by thermogravimetric analysis in Supporting Information Figure S4), the desodiation capacity gradually increases from 670 mAh/g_{composite} (~1585 mAh/g_P) in the first cycle to 711 mAh/g_{composite} (~1688 mAh/g_P) at the fifth cycle then maintains around 700 mAh/g_{composite} (~1660 mAh/g_P) during the rest of 50 cycles. It should be mentioned that the electrochemical performance shown in Figure 4c is tested in the electrolyte with FEC additive, which is used to improve the SEI film stability. For comparison, the red P–SWCNT composite is also tested in the electrolyte without FEC (1 M NaClO₄ in ethylene carbonate/dimethyl carbonate, 1:1 by volume) (Supporting Information Figure S5). As shown in Figure S5, the capacity of red P–SWCNT composite decays very fast in the electrolyte without FEC, indicating that FEC is necessary for the composite to achieve stable cycling performance. Figure 4d shows the Coulombic efficiency of different materials.

Pristine red P has a very low first cycle Coulombic efficiency of ~12%. For the red P/SWCNT mixture, the first cycle Coulombic efficiency increases to ~24%, probably due to the moderately improved conductivity by SWCNTs. The first cycle Coulombic efficiency of the red P–SWCNT composite is significantly improved to ~68%, much higher than that of red P and red P/SWCNT mixture. The Coulombic efficiency of the composite exceeds 95% after the first cycle, reaches over 99% after the 17th cycle, and remains stable during the rest of cycles. We notice that the first cycle Coulombic efficiency of our composite is somewhat lower than the values reported for amorphous P–carbon materials in the literature.^{27,28,32} This might be attributed to the fact that part of SWCNTs are not incorporated into the composite as shown in Supporting Information Figure S6 and these SWCNTs are expected to react with electrolyte to form SEI layer, lowering the first Coulombic efficiency of the composite. It is well-known that SWCNTs possess a very high specific surface area, and when SWCNTs are tested against sodium, the first cycle Coulombic efficiency is as low as ~8% (Figure 4d and Supporting Information Figure S3c).

Figure 4e presents the rate capability of the red P–SWCNT composite with the corresponding sodiation–desodiation curves plotted in Figure 4f. As shown in Figure 4e, the red P–SWCNT composite is able to deliver stable desodiation capacities of 700, 670, 640, 620, 590, 580, 500, and 300 mAh/g_{composite} at the current densities of 50, 100, 200, 300, 400, 500, 1000, and 2000 mA/g_{composite}. The great rate capability should be ascribed to the highly conductive network of SWCNTs, which is preserved during the nondestructive sample preparation process. As shown by the SEM (Figure 2) and TEM images (Figure 3), the SWCNTs not only cover but also penetrate bulk red P and distribute around small red P domains, providing fast and efficient electron transport during sodiation–desodiation reactions. Besides the cycling performance under the low current density of 50 mA/g_{composite} (Figure 4c), the extended cycling performance of red P–SWCNT composite under medium (500 mA/g_{composite} in Figure 4g) and high current densities (2000 mA/g_{composite} in Figure 4h) is also tested. When tested at the current density of 500 mA/g_{composite}, the red P–SWCNT composite shows almost no capacity decay during the recorded 200 cycles. The initial capacity increasing observed in Figure 4g might be attributed to the gradually reduced interface resistances, which include SEI resistance and charge transfer resistance, during the initial few cycles (see below Figure 5 and corresponding text). The red P–SWCNT composite presents excellent cycling performance when tested at 2000 mA/g_{composite} with 80% capacity retention after 2000 sodiation–desodiation cycles. The capacity fluctuation in Figure 4h might be due to the temperature

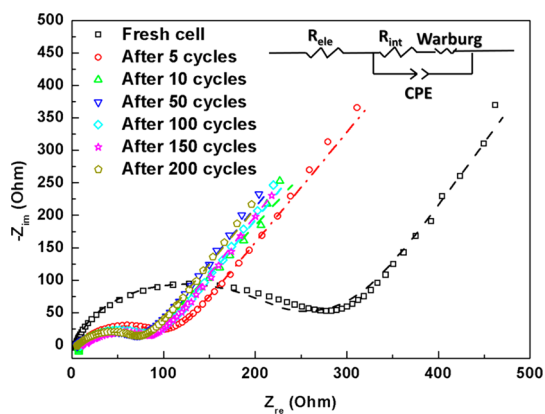


Figure 5. Nyquist plot of the red P–SWCNT composite cell before and after cycling with the inset showing the equivalent circuit used for data fitting (symbols, experimental data; dashed lines, fitting results).

variations during the electrochemical test, which was also reported in the literature.^{44,45} It is worth mentioning previous studies which showed that binders, such as PAA or carboxymethyl cellulose (CMC), need to be used to achieve the stable cycling performance of amorphous P–carbon materials because of the three-dimensional interconnection structure and high adhesive strength of those binders.^{28,29} When polyvinylidene fluoride (PVDF) was used as the binder, the electrochemical performance of amorphous P–carbon composite was unsatisfactory.^{28,29} In our case, conventional PVDF is used for the electrode preparation and the cycling performance of red P–SWCNT composite is comparable to the one reported in the literature using PAA or CMC binder, manifesting the intrinsic structure fortitude of the composite.

Electrochemical impedance spectroscopy (EIS) is used to investigate the mechanism for the stable cycling performance of red P–SWCNT composite. Figure 5 shows the Nyquist plots for red P–SWCNT composite after different sodiation–desodiation cycles. The Nyquist plot comprises a semicircle at medium frequency region and a straight line at low frequency region. The semicircle corresponds to sodium ions passing through the SEI film and charge transfer between electrolyte and active material, and the low frequency straight line is attributed to sodium ions diffusion inside active material. An equivalent circuit (inset of Figure 5), consisting of a resistor (R_{ele} , electrolyte resistance) and a constant phase element (CPE) in parallel with a resistor (R_{int} , interface resistance = SEI + charge transfer), which is connected with a Warburg element in series accounting for the sodium ion diffusion inside active material, is used to fit the impedance data. The obtained R_{ele} and R_{int} values are listed in Supporting Information Table S1. The value of R_{int} for fresh cell is 202 Ω , much smaller than the reported charge transfer resistance for P–MWCNTs

mixture prepared by hand-grinding.³³ After 5 cycles, R_{int} is reduced to 79 Ω and further decreased to 51 Ω at the 10th cycle, which might be the reason for the gradually increased capacity during the initial few cycles (Figure 4g). After 200 cycles, both R_{ele} and R_{int} are comparable to their values at the fifth cycle, indicating the stable interface between electrolyte and active material and explaining the stable cycling performance of the composite.

The formation of the stable interface between electrolyte and active material should be attributed to the remarkable mechanical properties of SWCNTs. As reported, the Young's modulus and tensile strength of SWCNTs can be as high as 1 TPa and 3.6 GPa, respectively, and CNTs can be repeatedly bent without introducing any plastic deformation.^{34,46,47} The stiff and flexible SWCNTs with exceptional strength can alleviate the sodiation–desodiation induced stress and provide a rigid skeleton for the composite, which preserve the electrode integrity and stabilize the SEI film during electrochemical cycling. As evidenced by the SEM images and the EDS elemental mapping for the cycled red P–SWCNT composite electrode (Supporting Information Figure S7), the electrode still maintains its structural integrity with few cracks observed after 2000 sodiation–desodiation cycles (Supporting Information Figure S7a). In the high magnification SEM image (Supporting Information Figure S7b), carbon nanotube bundles could be found on the surface of the composite particle. The SEM EDS elemental mapping in Figure S7d–f demonstrates that P and carbon still remains inseparable, indicating the robust structure of the composite.

CONCLUSION

In conclusion, we develop a red P–SWCNT composite by using a modified vaporization–condensation method with commercial red P and SWCNTs as starting materials. The red P–SWCNT composite is characterized by XRD, Raman, SEM and TEM. The results of XRD show that red P retains its crystalline structure in the composite and no surface interaction between red P and SWCNTs is detected by Raman. SEM and TEM images reveal that red P and SWCNTs are uniformly mixed together, and SWCNTs are randomly distributed around red P domains. Due to the nondestructive preparation method, the conductive network of SWCNTs is retained for the composite, enhancing the electric conductivity of the composite. Also, because of the fascinating mechanical properties of SWCNTs, the composite enables a stable interface between electrolyte and active material as evidenced by the EIS results. Benefiting from the improved conductivity and stabilized interface between electrolyte and active material, the composite presents a high overall sodium storage capacity, fast rate capability, and excellent long-term cycling performance with 80% capacity retention after

2000 sodiation–desodiation cycles, demonstrating that the red P–SWCNT composite prepared through

the modified vaporization–condensation method is a very promising anode for SIBs.

METHODS

Material Preparation. All chemicals are purchased from Sigma-Aldrich. Before any experiments, red P is washed with distilled water to remove surface oxide. For the preparation of red P–SWCNT composite, SWCNTs and red P with a weight ratio of 1:4 are hand-milled in a mortar for 15 min, and then sealed in a glass tube under vacuum condition. The glass tube is first heated to 600 °C and held for 2 h. Then, the temperature of the glass tube is decreased to 280 °C and held at this temperature for 48 h to convert white P to red P. After the glass tube naturally cools down to room temperature, it is taken out from the furnace and opened in an argon-filled glovebox. The P–SWCNT composite is collected and washed with carbon disulfide inside a glovebox to remove the white P generated during the condensation process. The red P–SWCNT sample is obtained by drying the after-washed P–SWCNT under 80 °C for 1 h inside vacuum oven. For comparisons, red P/SWCNT mixture is prepared by hand-grinding the SWCNTs and red P with a weight ratio of 6:4 in a mortar for 15, 30, or 45 min.

Material Characterizations. The crystal structures of samples are characterized by powder X-ray diffraction (XRD) on a D8 Advanced with LynxEye and SolX (Bruker AXS, Fitchburg, WI) using a Cu K α radiation source operated at 40 kV and 40 mA in the 2θ range of 10°–90° at the X-ray Crystallographic Center in University of Maryland. Raman spectra are collected on a Horiba Jobin Yvon Labram Aramis using a 532 nm diode-pumped solid-state laser at the Surface Analysis Center in University of Maryland. The morphologies of the samples are examined by both Hitachi SU-70 analytical ultrahigh resolution scanning electron microscope (SEM) and JEOL 2100F field emission transmission electron microscope (TEM) at the NanoCenter in University of Maryland. For the SEM EDS elemental mapping (Figure 2 and Supporting Information Figures S2 and S7), the samples are glued onto a piece of copper tape. After the test in Figure 4h is done, the cell is disassembled at a fully desodiated state inside an argon-filled glovebox, and before taking the images in Supporting Information Figure S7, the after-cycled electrode is rinsed with propylene carbonate to remove the salt residue on the electrode. Thermogravimetric analysis is used to determine the percentage of red P in the composite. The powder sample is loaded into the TGA equipment (SDT Q600, TA Instruments) and heated from room temperature to 800 °C in an argon atmosphere with a heating rate of 10 °C/min.

Electrochemical Tests. All electrodes are prepared under room atmosphere. The active material (red P, SWCNTs, red P/SWCNT mixture or red P–SWCNT composite) is manually mixed with PVDF in 1-methyl-2-pyrrolidinone (NMP) and carbon black in a weight ratio of 85:10:5 to form a slurry, which is then casted on copper foil with a doctor blade and dried in vacuum oven under 100 °C overnight. CR2032-type coin cells, with a Na foil counter electrode, a working electrode, Celgard 3501 microporous film separator, and 1.0 M NaClO $_4$ in FEC:dimethyl carbonate (DMC) (1:1 by volume) electrolyte, are assembled inside an argon-filled glovebox with both water and oxygen <0.5 ppm. The active materials loading on electrode is about 0.7–1.2 mg/cm 2 .

Cyclic voltammetry (CV) is tested from 0.001 to 2 V (vs Na/Na $^+$) under a scan rate of 0.05 mV/s. Galvanostatic charge–discharge tests are performed on an Arbin battery test station (BT2000, Arbin Instruments, College Station, TX). Coin cells are cycled between 0.001 and 2 V (vs Na/Na $^+$) under different current densities. After the cells reach the cutoff voltages, they are relaxed for 30 s before subsequent charge or discharge. For the tests in Figure 4g,h, the cells are precycled at 50 mA/g $_{\text{composite}}$ for certain cycles. For red P–SWCNT composite and red P/SWCNT mixture, both current densities and specific capacities are calculated on the basis of the total weight of red P–SWCNT composite or red P/SWCNT mixture. For red P and SWCNTs, both current densities and specific capacities are calculated on the

basis of the weight of red P or SWCNTs. Electrochemical impedance spectroscopy (EIS) tests with amplitude of 10 mV and frequency ranging from 10 6 to 0.1 Hz are performed on fresh cell and the same cell at fully desodiated states after different cycles. It is noteworthy to mention that the same cell is used for CV and EIS tests. After the fifth CV scan in Figure 4a, the cell is charged to 2.0 V (vs Na/Na $^+$) under a current density of 500 mA/g $_{\text{composite}}$ and held at this voltage for 10 h, followed by resting for 5 h. Then, EIS test is performed on the cell, and the result is denoted as “After 5 cycles” in Figure 5. Before any other EIS tests, the cell is galvanostatically charged–discharged between 0.001 and 2.0 V (vs Na/Na $^+$) at a current density of 500 mA/g $_{\text{composite}}$ until the number of cycle accumulates to certain value (5, 45, 95, 145, or 195 cycles). Subsequently, the voltage of the cell is held at 2.0 V (vs Na/Na $^+$) for 10 h followed by a 5 h relaxation. Then, EIS tests are performed on the cell, and the results are denoted as “After 10 cycles”, “After 50 cycles”, “After 100 cycles”, “After 150 cycles” and “After 200 cycles” in Figure 5, respectively. Both CV and EIS tests are recorded on Solatron 1260/1287 Electrochemical Interface (Solatron Metrology, U.K.).

Conflict of Interest: The authors declare no competing financial interest.

Supporting Information Available: The SEM and TEM images of pristine SWCNTs, the SEM image and EDS elemental mapping of red P/SWCNT mixture, the sodiation–desodiation profiles of different materials and the effect of hand-grinding time on the electrochemical performance of red P/SWCNT mixture, the TGA result of red P–SWCNT composite, the cycling stability of red P–SWCNT composite tested in FEC-free electrolyte, the SEM image and EDS elemental mapping of after-cycled red P–SWCNT composite electrode, and the resistances obtained from fitting experimental data in Figure 5 are shown in Figures S1–S7 and Table S1. This material is available free of charge via the Internet at <http://pubs.acs.org>.

Acknowledgment. This work was supported as part of the Nanostructures for Electrical Energy Storage (NEES), an Energy Frontier Research Center funded by the U.S. Department of Energy, Office of Science, Basic Energy Sciences under Award number DESC0001160. The authors acknowledge the technical support of the NanoCenter, X-ray Crystallographic Center, and Surface Analysis Center at the University of Maryland. The authors also thank Prof. Micheal R. Zachariah, Mr. Wenbo Zhou, and Ms. Lu Liu for their kind help on the TGA test.

REFERENCES AND NOTES

1. Tarascon, J.-M.; Armand, M. Issues and Challenges Facing Rechargeable Lithium Batteries. *Nature* **2001**, *414*, 359–367.
2. Slater, M. D.; Kim, D.; Lee, E.; Johnson, C. S. Sodium-Ion Batteries. *Adv. Funct. Mater.* **2013**, *23*, 947–958.
3. Palomares, V.; Villaluenga, I.; Hueso, K. B.; Carretero-Gonzalez, J.; Rojo, T. Na-Ion Batteries, Recent Advances and Present Challenges To Become Low Cost Energy Storage Systems. *Energy Environ. Sci.* **2012**, *5*, 5884–5901.
4. Kim, S.-W.; Seo, D.-H.; Ma, X.; Ceder, G.; Kang, K. Electrode Materials for Rechargeable Sodium-Ion Batteries. *Adv. Energy Mater.* **2012**, *2*, 710–721.
5. Yabuuchi, N.; Kubota, K.; Dahbi, M.; Komaba, S. Research Development on Sodium-Ion Batteries. *Chem. Rev.* **2014**, *114*, 11636–11682. doi:10.1021/cr500192f.
6. Yabuuchi, N.; Komaba, S. Recent Research Progress on Iron- and Manganese-Based Positive Electrode Materials for Rechargeable Sodium Batteries. *Sci. Technol. Adv. Mater.* **2004**, *15*, 043501(1–29).

7. Ge, P.; Fouletier, M. Electrochemical Intercalation of Sodium in Graphite. *Solid State Ionics* **1988**, *28–30*, 1172–1175.
8. Cao, Y.; Xiao, L.; Sushko, M. L.; Wang, W.; Schwenzler, B.; Xiao, J.; Nie, Z.; Saraf, L. V.; Yang, Z.; Liu, J. Sodium Ion Insertion in Hollow Carbon Nanowires for Battery Applications. *Nano Lett.* **2012**, *12*, 3783–3787.
9. Wen, Y.; He, K.; Zhu, Y.; Han, F.; Xu, Y.; Matsuda, I.; Ishii, Y.; Cumings, J.; Wang, C. Expanded Graphite as Superior Anode for Sodium-Ion Batteries. *Nat. Commun.* **2014**, *5*, 4033.
10. Nobuhara, K.; Nakayama, H.; Nose, M.; Nakanishi, S.; Iba, H. First-Principle Study of Alkali Metal-Graphite Intercalation Compounds. *J. Power Sources* **2013**, *243*, 585–587.
11. Kim, Y.; Ha, K.-H.; Oh, S. M.; Lee, K. T. High-Capacity Anode Materials for Sodium-Ion Batteries. *Chem.—Eur. J.* **2014**, *20*, 11980–11992.
12. Doeff, M. M.; Ma, Y.; Visco, S. J.; De Jonghe, L. C. Electrochemical Insertion of Sodium into Carbon. *J. Electrochem. Soc.* **1993**, *140*, L169–170.
13. Alcántara, R.; Jiménez-Mateo, J. M.; Lavela, P.; Tirado, J. L. Carbon Black: A Promising Electrode Material for Sodium-Ion Batteries. *Electrochem. Commun.* **2001**, *3*, 639–642.
14. Wenzel, S.; Hara, T.; Janek, J.; Adelmhelm, P. Room-Temperature Sodium-Ion Batteries: Improving the Rate Capability of Carbon Anode Materials by Templating Strategies. *Energy Environ. Sci.* **2011**, *4*, 3342–3345.
15. Tang, K.; Fu, L.; White, R. J.; Yu, L.; Titirici, M.-M.; Antonietti, M.; Maier, J. Hollow Carbon Nanospheres with Superior Rate Capability for Sodium-Based Batteries. *Adv. Energy Mater.* **2012**, *2*, 873–877.
16. Wu, L.; Buchholz, D.; Bresser, D.; Chagas, L. G.; Passerini, S. Anatase TiO₂ Nanoparticles for High Power Sodium-Ion Anodes. *J. Power Sources* **2014**, *251*, 379–385.
17. Wang, Y. S.; Yu, X. Q.; Xu, S. Y.; Bai, J. M.; Xiao, R. J.; Hu, Y. S.; Li, H.; Yang, X. Q.; Chen, L. Q.; Huang, X. J. Direct Atomic-Scale Confirmation of Three-Phase Storage Mechanism in Li₄Ti₅O₁₂ Anodes for Room-Temperature Sodium-Ion Batteries. *Nat. Commun.* **2013**, *4*, 2365.
18. Wu, D.; Li, X.; Xu, B.; Twu, N.; Liu, L.; Ceder, G. NaTiO₂: A Layered Anode Material for Sodium-Ion Batteries. *Energy Environ. Sci.* **2015**, *8*, 195–20210.1039/c4ee03045a.
19. Ellis, L. D.; Harchard, T. D.; Obrovac, M. N. Reversible Insertion of Sodium in Tin. *J. Electrochem. Soc.* **2012**, *159*, A1801–1805.
20. Xu, Y.; Zhu, Y.; Liu, Y.; Wang, C. Electrochemical Performance of Porous Carbon/Tin Composite Anodes for Sodium-Ion and Lithium-Ion Batteries. *Adv. Energy Mater.* **2013**, *3*, 128–133.
21. Xiao, L.; Cao, Y.; Xiao, J.; Wang, W.; Kovarik, L.; Nie, Z.; Liu, J. High Capacity, Reversible Alloying Reactions in SnSb/C Nanocomposites for Na-Ion Battery Applications. *Chem. Commun.* **2012**, *48*, 3321–3323.
22. Baggetto, L.; Allcorn, E.; Mathiram, A.; Weith, G. M. Cu₂Sb Thin Film as Anode for Na-Ion Batteries. *Electrochem. Commun.* **2013**, *27*, 168–171.
23. Qian, J.; Chen, Y.; Wu, L.; Cao, Y.; Ai, X.; Yang, H. High Capacity Na-Storage and Superior Cyclability of Nanocomposite Sb/C Anode for Na-Ion Batteries. *Chem. Commun.* **2012**, *48*, 7070–7072.
24. Zhu, Y.; Han, X.; Xu, Y.; Liu, Y.; Zheng, S.; Xu, K.; Hu, L.; Wang, C. Electrospun Sb/C Fibers for a Stable and Fast Sodium-Ion Battery Anode. *ACS Nano* **2013**, *7*, 6378–6386.
25. Stevens, D. A.; Dahn, J. R. The Mechanisms of Lithium and Sodium Insertion in Carbon Materials. *J. Electrochem. Soc.* **2001**, *148*, A803–811.
26. Extance, P.; Elliot, S. R. Pressure Dependence of the Electrical Conductivity of Amorphous Red Phosphorus. *Philos. Mag. B* **1981**, *43*, 469–483.
27. Qian, J.; Wu, X.; Cao, Y.; Ai, X.; Yang, H. High Capacity and Rate Capability of Amorphous Phosphorus for Sodium Ion Batteries. *Angew. Chem., Int. Ed.* **2013**, *52*, 4633–4636.
28. Kim, Y.; Park, Y.; Choi, A.; Choi, N.-S.; Kim, J.; Lee, J.; Ryu, J. H.; Oh, S. N.; Lee, K. T. An Amorphous Red Phosphorus/Carbon Composite as a Promising Anode Material for Sodium Ion Batteries. *Adv. Mater.* **2013**, *25*, 3045–3049.
29. Yabuuchi, N.; Matsuura, Y.; Ishikawa, T.; Kuze, S.; Son, J.-Y.; Cui, Y.-T.; Oji, H.; Komaba, S. Phosphorus Electrodes in Sodium Cells: Small Volume Expansion by Sodiation and the Surface-Stabilization Mechanism in Aprotic Solvent. *ChemElectroChem* **2014**, *1*, 580–589.
30. Wu, H.; Chan, G.; Choi, J. W.; Ryu, I.; Yao, Y.; McDowell, M. T.; Lee, S. W.; Jackson, A.; Yang, Y.; Hu, L.; Cui, Y. Stable Cycling of Double-Walled Silicon Nanotube Battery Anodes through Solid-Electrolyte Interphase Control. *Nat. Nanotechnol.* **2012**, *7*, 309–314.
31. Karki, K.; Zhu, Y.; Liu, Y.; Sun, C.-F.; Hu, L.; Wang, Y.; Wang, C.; Cumings, J. Hoop-Strong Nanotubes for Battery Electrode. *ACS Nano* **2013**, *7*, 8295–8302.
32. Song, J.; Yu, Z.; Gordin, M. L.; Hu, S.; Yi, R.; Tang, D.; Walter, T.; Regula, M.; Choi, D.; Li, X.; Manivannan, A.; Wang, D. Chemically Bonded Phosphorus/Graphene Hybrid as a High Performance Anode for Sodium-Ion Batteries. *Nano Lett.* **2014**, *14*, 6329–6335.
33. Li, W.-J.; Chou, S.-L.; Wang, J.-Z.; Liu, H.-K.; Dou, S.-X. Simply Mixed Commercial Red Phosphorus and Carbon Nanotube Composite with Exceptionally Reversible Sodium-Ion Storage. *Nano Lett.* **2013**, *13*, 5480–5484.
34. Yu, M. F.; Files, B. S.; Arepalli, S.; Ruoff, R. S. Tensile Loading of Ropes of Single Wall Carbon Nanotubes and Their Mechanical Properties. *Phys. Rev. Lett.* **2000**, *84*, 5552–5555.
35. Yu, M. F.; Lourie, O.; Dyer, M. J.; Moloni, K.; Kelly, T. F.; Ruoff, R. S. The Strength and Breaking Mechanism of Multiwalled Carbon Nanotubes under Tensile Load. *Science* **2000**, *287*, 637–640.
36. Li, F.; Cheng, B. S.; Su, G.; Dresselhaus, M. S. Tensile Strength of Single-Walled Carbon Nanotubes Directly Measured from Their Macroscopic Ropes. *Appl. Phys. Lett.* **2000**, *77*, 3161–3163.
37. Pan, Z. W.; Xie, S. S.; Lu, L.; Chang, B. H.; Sun, L. F.; Zhou, W. Y.; Wang, G.; Zhang, D. L. Tensile Tests of Ropes of Very Long Aligned Multiwall Carbon Nanotubes. *Appl. Phys. Lett.* **1999**, *74*, 3152–3154.
38. Marino, C.; Debenedetti, A.; Fraise, B.; Favier, F.; Monconduit, L. Activated-Phosphorus as New Electrode Material for Li-Ion Batteries. *Electrochem. Commun.* **2011**, *13*, 346–349.
39. Wang, L.; He, X.; Li, J.; Sun, W.; Gao, J.; Guo, J.; Jiang, C. Nano-Structured Phosphorus Composite as High-Capacity Anode Materials for Lithium Batteries. *Angew. Chem.* **2012**, *124*, 9168–9171.
40. Jesus, E. C.; Santiago, D.; Casillas, G.; Mayoral, A.; Magen, C.; Jose-Yacamán, M.; Li, J.; Cabrera, C. R. Platinum Electrodeposition on Unsupported Single Wall Carbon Nanotubes and Its Application as Methane Sensing Material. *J. Electrochem. Soc.* **2013**, *160*, H98–104.
41. Zaug, J. M.; Soper, A. K.; Clark, S. M. Pressure-Dependent Structure of Amorphous Red Phosphorus and the Origin of the First Sharp Diffraction Peaks. *Nat. Mater.* **2008**, *7*, 890–899.
42. Qian, J.; Qiao, D.; Ai, X.; Cao, Y.; Yang, H. Reversible 3-Li Storage Reactions of Amorphous Phosphorus as High Capacity and Cycling-Stable Anodes for Li-Ion Batteries. *Chem. Commun.* **2012**, *48*, 8931–8933.
43. Fuge, G. M.; May, P. W.; Rosser, S. R. J.; Ashfold, M. N. R. Laser Raman and X-Ray Photoelectron Spectroscopy of Phosphorus Containing Diamond-like Carbon Films Grown by Pulsed Laser Ablation Methods. *Diamond Relat. Mater.* **2004**, *13*, 1442–1448.
44. Hu, L.-H.; Wu, F.-Y.; Lin, C.-T.; Khlobystov, A. N.; Li, L.-J. Graphene-Modified LiFePO₄ Cathode for Lithium Ion Battery beyond Theoretical Capacity. *Nat. Commun.* **2013**, *4*, 1687.
45. Ramireddy, T.; Xing, T.; Rahman, M. M.; Chen, Y.; Dutercq, Q.; Gunzelmann, D.; Glushenkov, A. M. Phosphorus-Carbon Nanocomposite Anodes for Lithium-Ion and Sodium-Ion Batteries. *J. Mater. Chem. A* **2015**, *3*, 5572–558410.1039/C4TA06186A.

46. Falvo, M. R.; Clary, G. J.; Taylor, R. M., II; Chi, V.; Brooks, F. P., Jr.; Washburn, S.; Superfine, R. Bending and Buckling of Carbon Nanotubes under Large Strain. *Nature* **1997**, *389*, 582–584.
47. Knechtel, W. H.; Dusberg, G. S.; Blau, W. J.; Hernandez, E.; Rubio, A. Reversible Bending of Carbon Nanotubes Using a Transmission Electron Microscope. *Appl. Phys. Lett.* **1998**, *73*, 1961–1963.